communications earth & environment

Article

A Nature Portfolio journal

https://doi.org/10.1038/s43247-025-02778-0

Carbonate- and silicate-metasomatized mantle beneath Himalayan-Tibetan orogenic belt

Check for updates

Weikai Li [1,2,3], Zhiming Yang [1] ✉, Zoltán Zajacz [3], Limin Zhou[4] & Zengqian Hou [1]

The extreme geochemical enrichment of post-collisional potassium-rich lava in the Alpine-Himalayan orogenic belt has led researchers to hypothesize that enrichment is inherited from a metasomatized mantle source potentially incorporating crustal components. However, direct verification of metasomatic processes remains challenging due to the scarcity of mantle rocks preserving metasomatism records. Here, we report two groups of mantle xenolith entrained in Tibetan ultrapotassic lavas. Integrated petrographic observations, whole-rock geochemistry, and in-situ microanalysis reveal that subcontinental lithospheric mantle exhibits extreme enrichment in both isotopes and incompatible elements. Textural evidence of vein networks and melt pockets in xenoliths indicate the coexistence of carbonate and silicate metasomatic regimes. Considering subduction-collision background, we propose that the recycling of Indian continental materials during collision substantially contributes to the metasomatic enrichment of the Tibetan subcontinental lithospheric mantle.

The Alpine-Himalayan orogenic belt, extending over 15,000 km, represents the planet's longest collisional orogen. Post-collisional magmatism within this belt not only documents continental crustal thickening processes but also offers critical constraints on deep geodynamic mechanisms during subduction-collision orogeny[1], crust-mantle material recycling [2,3], and post-collisional mineralization[4,5]. Notably, mantle-derived post-collisional ultrapotassic lavas, defined by their geochemical criteria (K_2O > 3 wt%, MgO >3 wt%, K_2O/Na_2O > 2), exhibit extreme enrichment in incompatible elements and radiogenic isotopes[6–8]. These volcanic suites are predominantly interpreted as products of partial melting of metasomatized subcontinental lithospheric mantle, establishing them as vital archives for studying mantle enrichment processes in collisional orogeny [9–11].

Despite three decades of investigation, the petrogenetic origin of extreme geochemical enrichment in the sources of ultrapotassic magma remains contentious. Current debates center on two hypotheses: inheritance from pre-existing metasomatized mantle reservoirs versus acquisition through crustal assimilation during magma ascent. The former emphasizes the role of ancient mantle metasomatism by subduction-related fluids/melts[1,12], whereas the latter attributes enrichment to interaction with crustal materials during ascent[13,14]. Recent microanalytical investigations of Tibetan ultrapotassic lava phenocrysts revealed systematic decreases in Sr isotope ratios from early-formed crystal core to late-stage rim during fractionation crystallization[15], suggesting that the primary geochemical enrichment was source-inherited, with subsequent crustal interactions potentially modifying but not generating the observed signatures. The latest experimental petrology studies further demonstrate that subcontinental lithospheric mantle enrichment in orogenic settings results from interaction between depleted peridotite and recycled metasomatic agents, including hydrous pyroxenite-derived melts[16,17] and subducted sedimentary and/or crustal materials[18,19]. However, direct verification of metasomatism types and processes remains challenging due to the scarcity of mantle rocks preserving metasomatism records and the overprinting effects of post-magmatic processes.

Mantle xenoliths, as fragments of lithospheric mantle, typically retain robust geochemical evidence of ancient metasomatic events. This study presents comprehensive petrographic, whole-rock geochemical, and in-situ microanalytical investigations of peridotite and pyroxenite xenoliths entrained in southern Tibetan ultrapotassic lavas from the Himalayan-Tibetan orogenic belt. Our findings provide direct evidence for two types of

[1]State Key Laboratory of Deep Earth and Mineral Exploration, Institute of Geology, Chinese Academy of Geological Sciences, Beijing, China. [2]Department of Earth and Space Sciences, Southern University of Science and Technology, Shenzhen, China. [3]Department of Earth Sciences, University of Geneva, Geneva, Switzerland. [4]State Key Laboratory of Deep Earth and Mineral Exploration, National Research Center for Geoanalysis, Beijing, China.
✉e-mail: zm.yang@hotmail.com

mantle metasomatism (carbonate and silicate) through integrated multi-scale analysis.

Results and discussion

Sample and petrography

Twelve studied fresh xenoliths collected from southern Tibet (Supplementary Fig. S1 in the Supplementary Information file) can be categorized into two distinct groups: olivine (Ol)-rich group (ORG) and Ol-poor group (OPG). The ORG xenoliths (0.8–1.8 cm in diameter) include harzburgite, lherzolite, Ol-orthopyroxenite, and Ol-websterite (Figs. 1A, B and 2A), whereas the OPG xenoliths (1.2–3.5 cm in diameter) are exclusively websterite (Figs. 1C–H and 2A).

The ORG xenoliths display porphyroclastic textures dominated by subhedral olivine (27–53 vol.%) and orthopyroxene (Opx: 42–67 vol.%) grains (0.1–0.8 mm) with curvilinear boundaries (Fig. 1A). Orthopyroxene exhibits disequilibrium features indicated by BSE-dark cores rimmed by bright zones. Minor phases include clinopyroxene (Cpx), phlogopite (Phl), and spinel (Sp), with acicular apatite (Ap) locally occupying intergranular spaces. Notably, carbonates are identified in ORG xenoliths. They occur as: (1) mm-scale vein networks restricted to xenolith central part without penetrating the host rock (Supplementary Fig. S2), crosscutting coarse Ol and Opx grains while preferentially eroding Opx margins (Fig. 1B); (2) Ca-Mn-Ba-F-Cl-rich carbonate patches at grain boundaries (Fig. 1B and Supplementary Fig. S3).

The OPG websterites display protogranular to porphyroclastic texture mainly composed of coarse-grained Cpx (20–85 vol.%) and Opx (15–80 vol.%) with curved, rounded, and embayed texture indicative of disequilibrium (Fig. 1C–F). Compared with ORG, hydrous phase (e.g., phlogopite) is barely observed in OPG. Silicate and carbonate veins are very common in this group. The OPG websterites can be classified into two subtypes (type I, II) according to the type of veins they contain:

Type I websterite ($Cpx_{20\text{-}72}Opx_{24\text{-}80}Ol_{0\text{-}4}$): only contains Ca-Mn-Ba-K-Cl-rich carbonate vein networks transecting pyroxene (Fig. 1D and Supplementary Fig. S4).

Type II websterite ($Cpx_{59\text{-}85}Opx_{15\text{-}41}Ol_{0\text{-}4}$): characterized by silicate veins along the boundary of pyroxene (Fig. 1E), occasionally transecting pyroxene. Minerals in vein include plagioclase (Pl~90 vol.%), Opx (~5 vol.%), Fe-Ti oxide (~1 vol.%), and very minor Na-K-Al-Ti-rich glass without carbonate (Fig. 1F, G). Vein-pyroxene contacts show BSE-bright reaction zones with Cpx dissolution textures (Fig. 1F, G). These silicate veins frequently connect vermicular silicate pockets at triple junctions, comprising glass (45 vol.%), fine-grained Opx (45 vol.%), Cpx (5 vol.%), and minor Fe-Ti oxides (Fig. 1H). Neither carbonate nor silicate veins/pocket are observed in the host lava.

Whole-rock compositions

The ORG xenolith suite exhibits distinct geochemical characteristics compared to OPG, displaying significantly elevated whole-rock Mg# values (87–89), MgO contents (33.6–35.9 wt%), and compatible element concentrations (Ni = 1143–1898 ppm; Cr = 1542–2510 ppm). Conversely, ORG xenoliths show relatively depletion in TiO_2, Al_2O_3, K_2O, CaO, Li, and heavy rare-earth elements (HREEs) as documented in Fig. 2B, Supplementary Fig. S5 and Supplementary Data 1. Within the OPG group, type I websterites demonstrate slightly higher MgO, TiO_2, and K_2O contents relative to type II (Fig. 2B and Supplementary Fig. S5).

All analyzed xenoliths share coherent chondrite-normalized REE patterns characterized by strong light REE (LREE) enrichment relative to HREE and consistent negative Eu anomalies (Fig. 2C). Primitive mantle-normalized trace element diagram is characterized by pronounced negative Ba, Nb, Ta, and Ti anomalies (Fig. 2D). Large ion lithophile elements (LILE: Rb, Ba, K) enrichment contrasts with high field strength elements (HFSE: Nb, Ta, Zr, Hf, Ti) depletion, forming characteristic "arc-type" signatures. The host volcanic rocks exhibit nearly identical trace element patterns to the xenolith, suggesting cogenetic relationships between mantle xenoliths and their carrier magmas.

Whole-rock $^{87}Sr/^{86}Sr$ and $^{143}Nd/^{144}Nd$ ratios of ORG range from 0.716775 to 0.718698, 0.511868 to 0.511913, respectively (Fig. 2E). The OPG has slightly lower but more concentrated $^{87}Sr/^{86}Sr$ ratios (0.715648–0.176066) within a wide variation of $^{143}Nd/^{144}Nd$ (0.511862–0.512006). The $^{87}Sr/^{86}Sr$ positively correlates with $(La/Yb)_N$ ratio in both groups (Fig. 2F).

Mineral compositions

Olivine from ORG has higher Fo value (84–87), Ni, incompatible elements concentration (e.g., Li, K, Ba, P, Sr, Zr), and lower CaO content (0.04–0.09) than Ol phenocrysts from host rock (Fig. 3A–D and Supplementary Data 2). Olivine compositions from OPG remain unavailable due to the scarcity and small size of olivine crystals.

The Al_2O_3, CaO, and Na_2O contents in Cpx increase with decreasing of MgO (Fig. 4A–C). The Cpx in both ORG and OPG displays higher Li concentration than Cpx phenocryst from host rock (Fig. 4D). All Cpx display upward-convex REE patterns with negative Eu anomalies (Fig. 4E). Primitive mantle-normalized pattern of Cpx is similar to whole rock (Fig. 4F). Most Cpx from ORG are enriched in Ba concentration compared to those from OPG, resulting in higher Ba/La ratio (Fig. 4G). The Cpx in ORG and OPG-type I websterite plot in carbonatite metasomatism field (Fig. 4H). In contrast, Cpx in one type II websterites (C01) shows a silicate metasomatism trend with high Ti/Eu ratio (Fig. 4H), while Cpx in the other two type II websterites (C02, C03) have the highest Ti/Eu and $(La/Yb)_N$ ratio. In OPG, Cpx in direct contact with silicate vein or pocket has higher Ti, Na, HREE, Sr, Zr than those not in contact (Supplementary Fig. S6).

In-situ $^{87}Sr/^{86}Sr$ values of Cpx from ORG (0.7169–0.7204) are higher than that from OPR (0.7135–0.7148; Fig. 4I). In both ORG and OPG, $^{87}Sr/^{86}Sr$ ratio positively correlates with $(La/Yb)_N$ in Cpx ($R^2 = 0.82$ and 0.77). The Sr isotope data of Cpx in type I websterite are not available owing to the large errors ($2\sigma \geq 0.001$), which is probably caused by the small size and disequilibrium texture.

Overall, Tibetan peridotite and pyroxenite xenoliths demonstrate pronounced geochemical enrichment.

Origin of ORG and OPG

Two fundamental questions inevitably arise when investigating the petrogenesis of mantle-derived xenoliths, particularly pyroxenite: (1) Are these lithologies primary mantle formations or products of melt segregation during upwelling? (2) Does their geochemical enrichment originate from mantle metasomatism or magmatic process? While incompatible elements typically concentrate in residual melts and late-stage crystallizing phases during fractionation crystallization, our analyses reveal a clear geochemical paradox. Coarse-grained Ol in ORG xenolith have obviously higher incompatible element concentrations (e.g., Li, Ba, K, P, Sr, Zr, Hf, Th) compared to phenocrysts in the evolved host lava (Fig. 3). Similarly, coarse-grained Cpx in both OPG and OPG has higher Li coupled with higher Mg# value relative to Cpx phenocryst (Fig. 4D). This geochemical dichotomy contradicts conventional expectations for crystal segregation from a common magma source. Post-magmatic processes such as crustal assimilation or mixing with enriched end-members cannot adequately account for these observations, as they fail to explain the selective enrichment of xenoliths compared to their host lavas. This interpretation is further strengthened by petrological and isotopic evidence showing that most crustal xenoliths are relatively depleted than the host ultrapotassic lava[12,15,20]. Hence, one of convincing interpretations is that ORG and OPG xenoliths represent fragments of mantle sources that experienced pre-entrainment metasomatic enrichment.

Two types of metasomatism and corresponding impacts

Peridotite and pyroxenite in ORG and OPG show wide variations in modal and chemical compositions. Such a heterogeneity can be primarily ascribed to two distinct petrogenetic processes: (1) differential melt extraction from an initially enriched pyroxenite protolith, and (2) polyphase metasomatic overprinting of peridotite precursors by infiltrating melts. As discussed

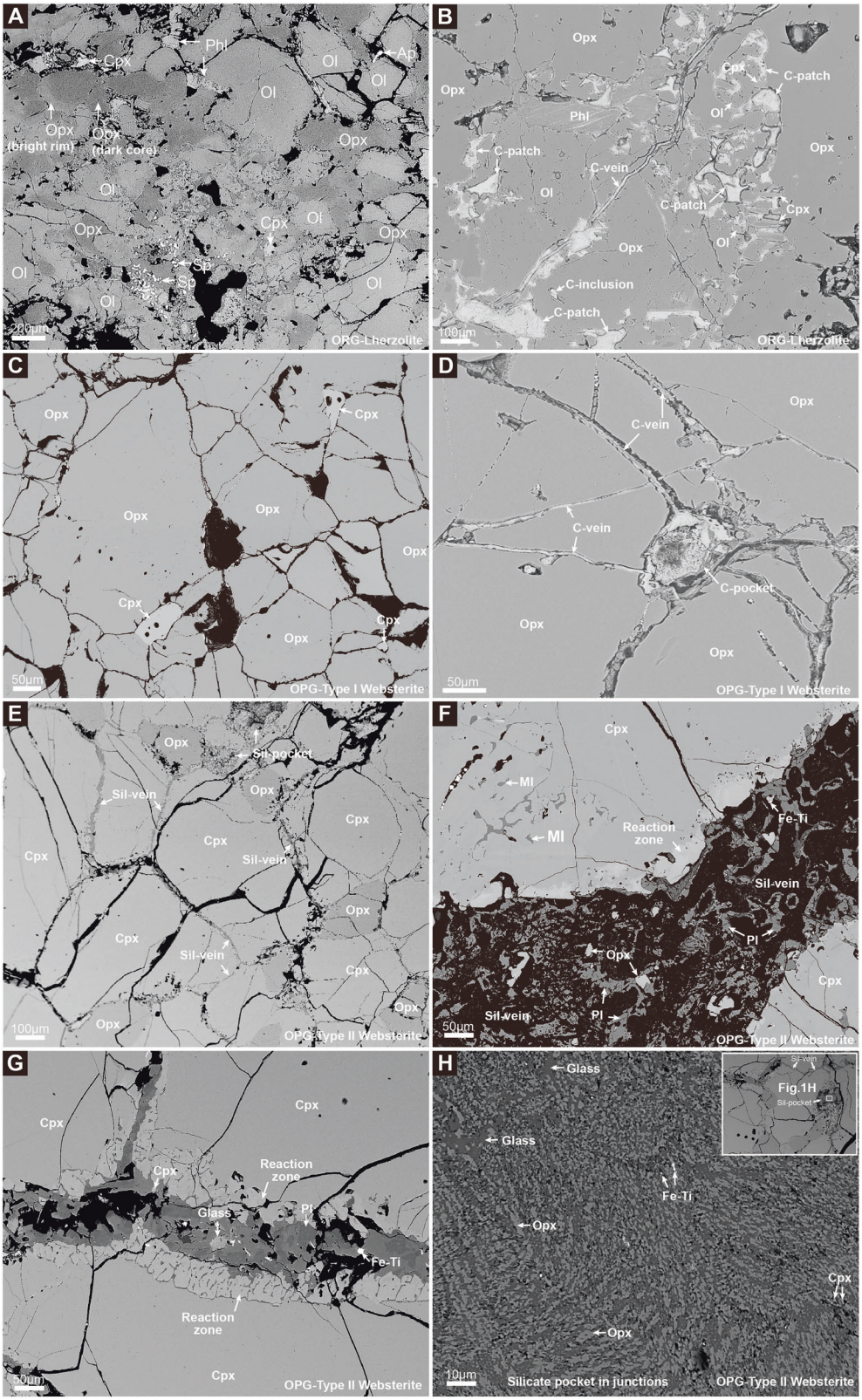

Fig. 1 | Back scattered electron (BSE) images of ORG and OPG mantle xenoliths. **A** BSE image showing minerals in ORG. **B**, **D** BSE images showing carbonate veins, patches, and inclusions in ORG and OPG xenolith, respectively. **C** BSE image showing minerals in OPG. **E**–**G** Structure and mineral assemblage of silicate veins in OPG. **H**: Mineral assemblage in silicate pocket. Abbreviations: Ap apatite, C carbonate, Cpx clinopyroxene, Ol olivine, Opx orthopyroxene, Phl phlogopite, Pl plagioclase, Sil silicate, Sp spinel.

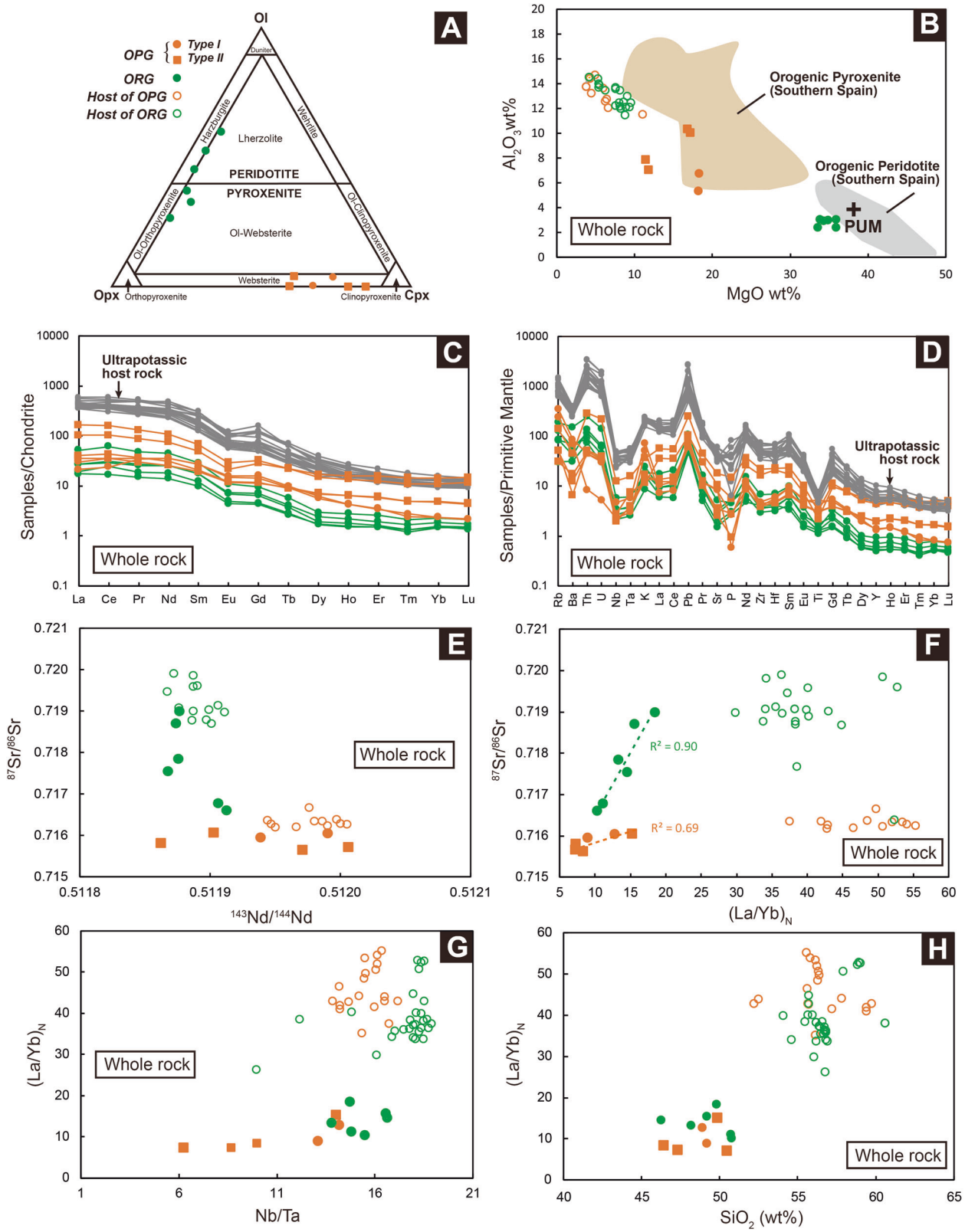

Fig. 2 | Whole-rock geochemical features of mantle xenoliths and ultrapotassic host rocks. A Ol-Opx-Cpx triangular plot for peridotites and pyroxenite xenoliths. **B** MgO (wt%) vs. Al_2O_3 (wt%) diagram. Values of primitive upper mantle (PUM) are collected from ref. 30. **C** Chondrite-normalized REE patterns. **D** Primitive mantle-normalized multielement patterns. The values for chondrite and primitive mantle were taken from ref. 42. **E** $^{143}Nd/^{144}Nd$ vs. $^{87}Sr/^{86}Sr$ ratios diagram. **F** $(La/Yb)_N$ vs. $^{87}Sr/^{86}Sr$ ratios diagram. In xenoliths of OPG and ORG, $(La/Yb)_N$ ratios show strong positive correlation with $^{87}Sr/^{86}Sr$ ratios, $R^2 = 0.69$ and 0.90, respectively. **G** Nb/Ta vs. $(La/Yb)_N$ ratios. **H** SiO_2 (wt%) vs. $(La/Yb)_N$ ratios. The data source is Supplementary Data 1.

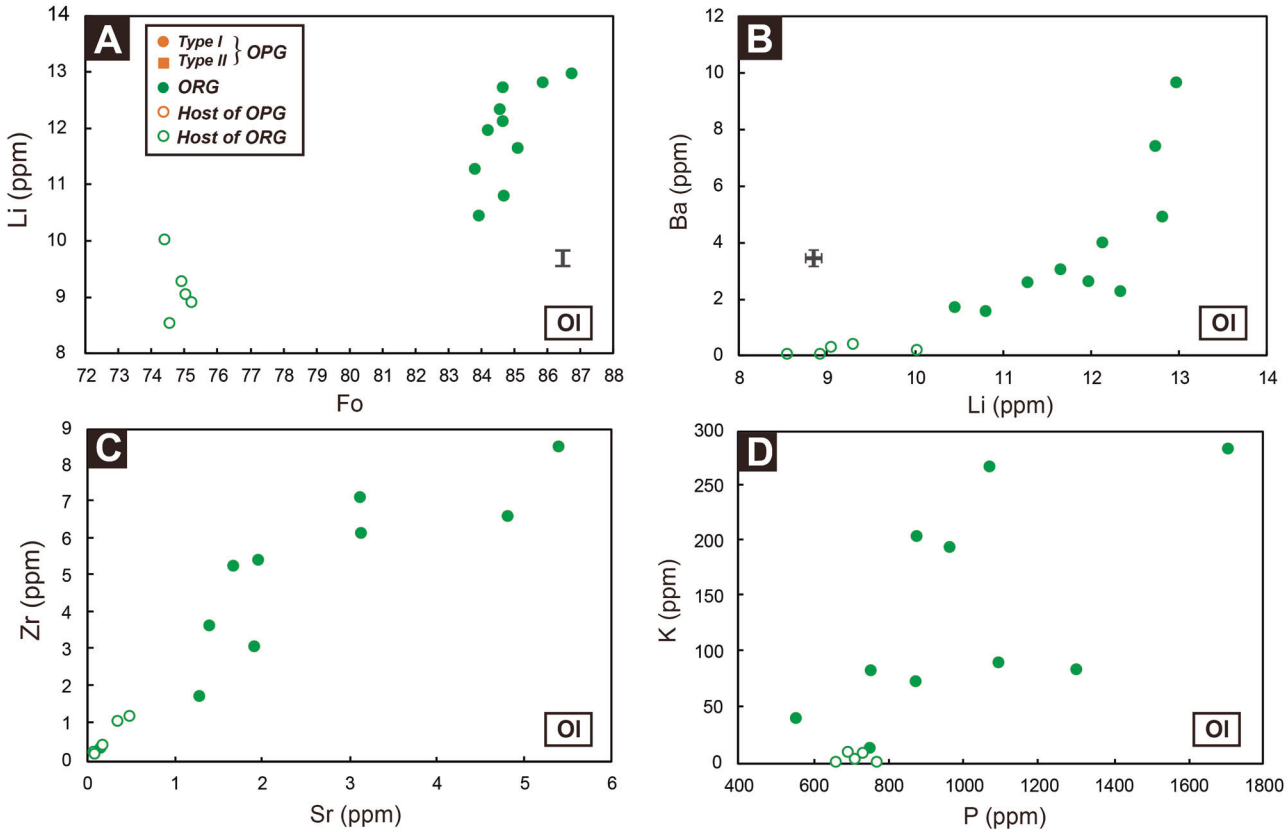

Fig. 3 | Geochemical features of olivine in mantle xenoliths and ultrapotassic host rocks. **A** Fo content (mol%) vs. Li (ppm) of olivine in ORG xenolith and olivine phenocryst in host rock. Fo=Mg/(Mg+ Fe) molar ratio. **B** Li (ppm) vs. Ba (ppm) contents of olivine in ORG xenolith and host rock. **C** Sr (ppm) vs. Zr (ppm) contents of olivine in ORG xenolith and host rock. **D** P (ppm) vs. K (ppm) contents of olivine in ORG xenolith and host rock. Data source is Supplementary Data 2.

below, the first mechanism can be ruled out, and we favor the second mechanism.

The systematic negative correlation between MgO and other oxides in both whole rock and Cpx has been widely recognized as geochemical indicator for melt extraction of mantle rock. Oxides and modal Cpx contents seem to be elevated with decreasing of MgO and Mg# from ORG to OPG, but this trend is discontinuous between two groups (Fig. 2B and Supplementary Fig. S5). The Al_2O_3, Na_2O, and CaO contents in Cpx roughly increase with decreasing of MgO (Fig. 4A–C), might indicative of enhanced melt extraction efficiency from OPG to ORG. Theoretically, melt extraction in compositionally homogeneous mantle sources would not substantially alter the isotopic signature of residual lithologies. However, Sr-Nd isotope of ORG and OPG is notably different (Fig. 2E). This fundamental discrepancy necessitates consideration of additional petrogenetic factors.

Porphyroclastic texture observed in mantle rock is commonly interpreted to reflect infiltration of fluid and/or melt[21]. In the Tibetan subcontinental lithospheric mantle, carbonate- and silicate-bearing veins/pockets provide critical evidence for metasomatic events. Three lines of evidence argue against a genetic link between these features (of vein/pocket) and host melts: (1) their restricted occurrence within xenoliths, (2) mineralogical discrepancies with host rocks (Fig. 1 and Supplementary Fig. S2), and (3) textural characteristics consistent with mantle P-T condition melt-rock reactions. The carbonate-bearing veins and pockets, exemplified by fine-grained Cpx+Opx+Ol+carbonate assemblages and carbonate-embayed Opx textures (Fig. 1B), document carbonate melt-peridotite/pyroxenite reactions through Opx dissolution: Opx+Carbonate→Cpx+Ol+CO_2[8]. This interpretation is supported by the former observation of CO_2-rich fluid inclusions in Tibetan peridotite xenoliths[22]. Moreover, partial melts and residues from carbonate metasomatism sources are considered to inherit elevated $(La/Yb)_N$ and Nb/Ta ratios coupled with reduced Ti/Eu ratios, reflecting carbonate melt infiltration processes[23,24]. In carbonate-bearing xenoliths (ORG and OPG-type I websterite), the concordance between petrographic features and geochemical signatures (Fig. 4H) confirms carbonate metasomatism imprinting. Note that the $(La/Yb)_N$ vs. Ti/Eu diagram is designed to discriminate between carbonate and silicate metasomatism in mantle peridotites. However, given ongoing debates regarding pyroxenite petrogenesis, particularly the prevailing model that pyroxenites form through hybridization reactions between peridotites and enriched heterogeneous end-members, clinopyroxenes in pyroxenites may retain signatures of both their peridotitic precursors and metasomatic overprinting by heterogeneous components. Therefore, pyroxenite data are retained here for comparative context.

In addition, the enrichment of fluid-mobile elements (Ba, F, Cl) in carbonates (Supplementary Figs. S3 and S4) indicates fluid-rich carbonate metasomatism, consistent with elevated Cpx Ba/La ratios (Fig. 4G). Nevertheless, the source of the infiltrating carbonate melt remains unclear.

For silicate-bearing vein and pocket in OPG (type II), the residue small glass fragment provides direct evidence of silicate melt infiltration. The dissolved Cpx in reaction zone further attest to melt impregnation and interaction[25–27]. The Cpx that interfaces with veins/pockets exhibits Ti, Na, Sr, Zr, and HREE enrichment relative to those not in contact (Supplementary Fig. S6), reflecting elemental contributions from infiltrating silicate melts. The presence of Fe-Ti oxides in veins additionally indicates Fe-Ti-rich melt compositions. However, Pl precipitation within these features appears inconsistent with the systematic negative Eu anomalies observed in whole-rock and mineral analyses (Figs. 2C and 4E). Given the lack of Eu enrichment in silicate veins/pockets relative to the

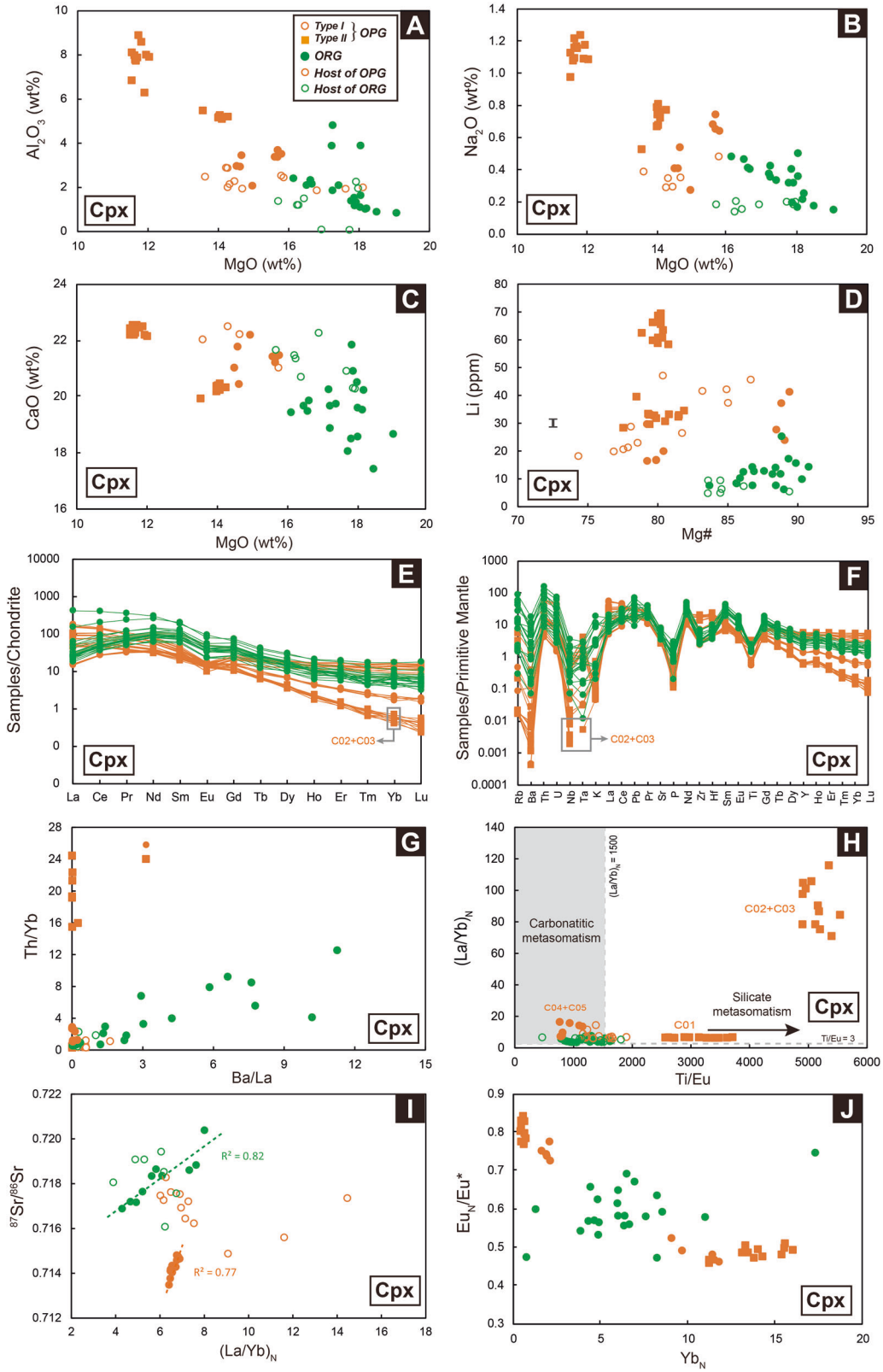

Fig. 4 | Geochemical features of clinopyroxene in mantle xenoliths and ultrapotassic host rocks. **A** MgO (wt%) vs. Al_2O_3 (wt%) of clinopyroxene from both xenolith and phenocryst in host rock. **B** MgO (wt%) vs. Na_2O (wt%) of clinopyroxene. **C** MgO (wt%) vs. CaO (wt%) of clinopyroxene. **D** Mg# value vs. Li (ppm) contents of clinopyroxene. **E** Chondrite-normalized REE patterns of clinopyroxene. **F** Primitive mantle-normalized multielement patterns of clinopyroxene. The values for chondrite and primitive mantle were taken from ref. 42. **G** Ba/La vs. Th/Yb ratios of clinopyroxene from xenolith and phenocryst in host rock. **H** Ti/Eu vs. $(La/Yb)_N$ ratios diagram of clinopyroxene. The carbonatite metasomatism field is Ti/Eu<1500, $(La/Yb)_N > 3$ (ref. 43.). **I** $(La/Yb)_N$ vs. $^{87}Sr/^{86}Sr$ ratios diagram. In xenoliths of OPG and ORG, $(La/Yb)_N$ ratios show strong positive correlation with $^{87}Sr/^{86}Sr$ ratios, $R^2 = 0.77$ and 0.82, respectively. **J** Yb_N vs. Eu_N/Eu^* ratio of clinopyroxene. N indicates chondrite normalized after ref. 42. $Eu^* = Eu_N/(Sm_N+Gd_N)^{1/2}$. Gray error bars represent the mean error of the parameters on both axes, those with ranges smaller than the size of data points are not displayed on figures. Data source is Supplementary Data 3.

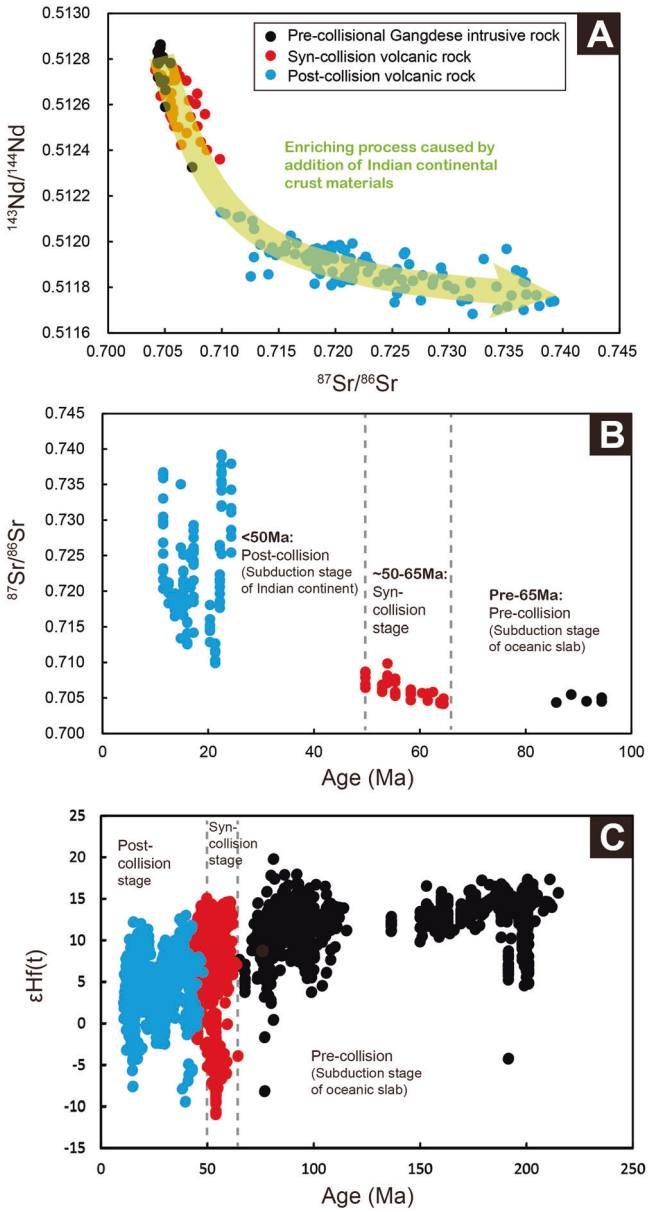

Fig. 5 | Temporal Sr-Nd and Hf isotopic evolution of Tibetan magmatism shows a clear enrichment trend from pre-collisional to post-collisional stages. **A** $^{87}Sr/^{86}Sr$ vs. $^{143}Nd/^{144}Nd$ ratios of whole-rock data. Whole-rock data include typical Late Cretaceous Gangdese arc magma formed before collision (>65 Ma), volcanic lava erupted during collision (~50–65), and mantle-derived volcanic lava formed after collision (<50 Ma). **B** Age (Ma) vs. $^{87}Sr/^{86}Sr$ ratios. Data are collected from refs. 2,7,8. **C** Age (Ma) vs. εHf(t) values. Data are collected from ref. 44.

pyroxenite (Supplementary Fig. S7), three mechanisms potentially resolve this paradox: (1) Pre-infiltration Pl fractionation: Early crystallization of Eu-rich Pl before infiltration results in depletion of Eu in later infiltrating melt. (2) Alkaline melt derivation: Pl crystallization from a Ca-poor Na-K-rich infiltrating melt would suppress Eu-Ca substitution. This is supported by Na and K enrichment relative to Ca in silicate vein and pocket (Supplementary Fig. S7). (3) Subsolidus re-equilibration: Cpx-Pl re-equilibration in the Pl stability field is thought to typically cause Eu depletion and HREE enrichment in Cpx because HREE is more readily concentrated in Cpx[27,28]. Yet the absence of clearly negative Eu_N/Eu^*-Yb_N correlations within type II websterite of OPG negate this process (Fig. 4J). Collectively, these observations suggest the cryptic metasomatism recorded by silicate veins/pockets likely originated from Fe-Ti-rich alkaline silicate melts.

Deep processes controlling metasomatism and geological implications

In addition to elemental enrichment from silicate metasomatism, carbonate metasomatism contributes isotopically as evidenced by strong positive correlations between $^{87}Sr/^{86}Sr$ ratios and $(La/Yb)_N$ values in both whole-rock samples ($R^2 = 0.69$ and 0.90; Fig. 2F) and clinopyroxenes ($R^2 = 0.77$ and 0.82; Fig. 4I). The absence of correlations between $(La/Yb)_N$ and SiO_2 (Fig. 2H) effectively excludes partial melting or magmatic differentiation as potential mechanisms. Although elevated $(La/Yb)_N$ ratios typically characterize carbonate metasomatism, potential contributions from silicate metasomatism and associated pyroxenite-forming processes in the deep mantle still require consideration. The Cpx in the two websterites (C02, C03) exhibit extremely high $(La/Yb)_N$ ratios (71–116; Fig. 4H) coupled with high Sr/Y ratios (20–22; Supplementary Data 3). This probably indicates that the source of Tibetan pyroxenite involves a deep-seated endmember with strong garnet segregation because these high ratios are attributed to low Yb (0.07–0.12 ppm) and Y concentration (2.61–3.03 ppm) rather than La and Sr enrichment (Fig. 4E, F and Supplementary Data 3). Silicate metasomatism represented by silicate vein and pocket is not responsible for this because of their HREE-rich feature (Supplementary Fig. S7). In this context, the positive correlation of $(La/Yb)_N$ and Sr/Y with $^{87}Sr/^{86}Sr$ ratios (Figs. 2F and 4I) imply variable contributions from this garnet-fractionated source, though its genetic relationship with infiltrating melts remains ambiguous. Moreover, the extremely low Nb (<0.06 ppm) and Ta (<0.001 ppm) contents in Cpx from C02 and C03 (Fig. 4F and Supplementary Data 3) further require the presence of rutile as a residual phase in the source region, due to the strong preferential partitioning of Nb and Ta into rutile.

Participation of such a garnet-, Pl- and rutile-bearing endmember generally indicates a high-pressure melting condition[29]. The subduction-related geochemical fingerprint (e.g., LILE enrichment and HFSE depletion; Figs. 2D and 4F) combined with the high Li concentration (Figs. 3A, B and 4D) strongly implicates subducted Indian continental crust as one of the probable deep endmembers. Lithium abundances in the studied pyroxenite xenoliths (21.3–36.4 ppm; Supplementary Data 1) significantly exceed typical mantle values (<2 ppm; ref. 30.) and oceanic lavas (<10 ppm; ref. 31.), aligning better with continental crustal reservoirs (~24 ppm; ref. 32.) and clastic sediments (~70 ppm; ref. 11.). The temporal isotopic evolution of Tibetan magmatism reveals a pronounced enrichment from the pre-collisional (pre-65 Ma) to post-collisional stages (Fig. 5), a pattern that coincides with seismic evidence for the northward underthrusting of Indian continental crust beneath the study area as revealed by the seismic data[33]. We therefore propose that the recycling of Indian continental materials during collision substantially contributes to the metasomatic enrichment of the Tibetan subcontinental lithospheric mantle.

Methods

Prior to wet chemistry analysis, xenolith samples underwent repeatedly grinding-polishing using a precision mill under binocular and microscope to completely remove contamination from adhered host rock. Trace element compositions of coarse Ol in ORG and Cpx from both xenolith groups were determined by laser ablation inductively coupled plasma mass spectrometry (LA-ICP-MS). In-situ Sr isotope ratios in Cpx were determined by using a multi-collector ICP-MS (MC-ICP-MS) interfaced with a femtosecond laser ablation system.

Trace elements analysis by LA-ICP-MS

The LA-ICP-MS was employed to determine trace element concentrations in olivine, clinopyroxene from xenoliths and ultrapotassic host rocks at the University of Tasmania. The system consisted of a New Wave Research UP213 Nd-YAG (213 nm) laser coupled to an Agilent 7900 quadrupole mass spectrometer. Ablation was conducted using 30–60 μm diameter spots at a repetition rate of 10 Hz. Data reduction followed the standard methods of ref. 34, with NIST612 glass as the primary reference material and USGS BCR-2G glass as the secondary standard. Analytical results are presented in Supplementary Data 2 and 3.

Major elements analysis by EMPA

Clinopyroxene major element compositions were analyzed using a JEOL JXA-8230 Superprobe electron microprobe at the Institute of Mineral Resources, Chinese Academy of Geological Sciences (CAGS). Operating conditions included an accelerating voltage of 15 kV, a probe current of 20 nA, and a beam diameter of 2–5 μm. Calibration utilized synthetic oxides and natural mineral standards, with matrix effects corrected via the manufacturer-supplied ZAF procedure. The detection limits ranged from 77 to 244 ppm, and measurement accuracy was maintained within 5% relative error. Complete major element data for Cpx are provided in Supplementary Data 3.

In-situ Sr isotope analysis

In-situ Sr isotope measurements of clinopyroxene were performed using a Neptune Plus MC-ICP-MS (Thermo Fisher Scientific, Germany) at the National Research Center for Geoanalysis, Chinese Academy of Geological Sciences. The system was coupled to a J-200 343 nm Yb-fiber femtosecond laser ablation system (Applied Spectra, USA). A baffled-type smoothing device was used before MC-ICP-MS to reduce the fluctuation effect induced by laser-ablation pulses and improve the quality of data. Instrument modifications included a high-efficiency dry pump for enhanced ion transmission and JET/X skimmer cones with a guard electrode. All measurements were conducted under low resolution and static mode. The NBS987 standard yielded $^{87}Sr/^{86}Sr = 0.710245 \pm 0.000025$ (2σ, $n = 32$), consistent with TIMS values (0.710236; ref. 35.). The analysis was optimized with NIST 612 to achieve maximum signal intensity and low oxide rates. The electronic baseline of every Faraday collector and gain for each amplifier were determined and calibrated. The clinopyroxene grains were ablated in line mode with spot size of 20–40 μm, line length of 20–40 μm, sample stage movement speed of 0.65 μm/s, laser repetition rate of 2–10 Hz, and beam energy density of ~1 J/cm^2. The instrumental mass bias for Sr isotopes was corrected using an exponential law function based on the $^{86}Sr/^{88}Sr$ value of 0.1194. The correction of interferences of Kr isotopes (impurities in the Ar gas) on mass 84 and 86 was successfully accomplished by the background subtraction. The interferences of Rb and doubly charged ions of Er and Yb on Sr were corrected based on the measured signal intensities of ^{85}Rb, $^{167}Er^{2+}$, and $^{173}Yb^{2+}$ and their natural isotopic relative abundances[36–38]. The Durango apatite standard and the StHs6 80-G glass standard were analyzed to monitor the instrument stability, yielding a mean value of $^{87}Sr/^{86}Sr = 0.70655 \pm 0.00046$ (2σ, $n = 19$; the recommended value by TIMS is 0.70640 ± 0.00007; ref. 39) and $^{87}Sr/^{86}Sr = 0.70348 \pm 0.00011$ (2σ, $n = 7$; recommended value by TIMS is 0.703497 ± 0.000034; ref. 40), respectively. Data are reported in Supplementary Data 3. As the $^{87}Rb/^{86}Sr$ ratios of all analyzed clinopyroxene were very low and the age of the host is relatively young (<20 Ma; ref. 2.), the $^{87}Sr/^{86}Sr$ ratios were not age-corrected.

Whole-rock major and trace element analysis

Fresh peridotite and pyroxenite xenoliths were selected under the binocular. Then they were repeatedly polished by grinder and carefully checked under binocular and microscope in order to remove all attached host rock part completely. Ultrapotassic host rocks were ground to remove surfaces, cleaned with deionized water, crushed, and powdered in an agate mill. Wet chemical analyses were carried out at Activation Laboratories Ltd. Sample powder was mixed with a flux of lithium metaborate and tetraborate, and fused in an induction furnace. The molten mixture was poured into a 5% nitric acid solution containing an internal standard, and mixed continuously until completely dissolved (~30 min). Major and selected trace elements (e.g., Ba, Sr, and V) were analyzed by ICP–MS (Thermo Jarrell-Ash ENVIRO II ICP or Varian Vista 735 ICP), with reference materials NIST694, DNC1, GBW07113, NIST1613b, SY4, and BIR-1a being analyzed in parallel. Analytical precisions were 1%–2%. Accuracy for major elements, as determined by reproducibility of standard and duplicate analyses, was typically within ±5% (≤±3% for SiO_2 and Al_2O_3). Trace element analyses involved digestion of sample powder in aqua regia with reference materials for the metals of interest. Samples and standards were analyzed by ICP–MS (Perkin Elmer Sciex 9000). Accuracy for trace elements was within ±10%. More detailed methods are available from Actlabs (http://www.actlabs.com). The analyzed data are listed in Supplementary Data 1.

Whole-rock Sr isotope analysis

Fifty milligrams of sample powder were digested over three days on a hot-plate (120 °C), with HF and HNO_3 in 15 ml PFA screw vials for three days. Then the digested sample was dried and the residue was dissolved in 1.5 ml 3 M HNO_3 and centrifuged. A fraction of the sample solution was loaded onto the column with SR-Spec resin[41] to separate Sr. The $^{87}Sr/^{86}Sr$ ratios were determined with a Neptune Plus MC-ICP-MS in the National Research Center for Geoanalysis, CAGS. The NBS 987 Sr isotopic standard solution was determined, and yielded the $^{87}Sr/^{86}Sr$ value of 0.710235 ± 0.000025 (2σ, $n = 10$). The analyzed data are listed in Supplementary Data 1.

Data availability

The data required to produces all figures are available in the supplementary data files.

Received: 23 May 2025; Accepted: 9 September 2025;
Published online: 16 October 2025

References

1. Prelević, D. et al. Ultrapotassic mafic rocks as geochemical proxies for post-collisional dynamics of orogenic lithospheric mantle: the case of southwestern Anatolia. *Turkey. J. Petrol.* **53**, 1019–1055 (2012).
2. Guo, Z., Wilson, M., Dingwell, D. B. & Liu, J. India-Asia collision as a driver of atmospheric CO_2 in the Cenozoic. *Nat. Commun.* **12**, 3891 (2021).
3. Du, D. H. et al. A recipe for making potassium-rich magmas in collisional orogens: New insights from K and Fe isotopes. *Earth Planet. Sci. Lett.* **632**, 118642 (2024).
4. Richards, J. P. & Şengör, A. C. Did Paleo-Tethyan anoxia kill arc magma fertility for porphyry copper formation? *Geology* **45**, 591–594 (2017).
5. Yang, Z. M., Goldfarb, R. & Chang, Z. S. Generation of postcollisional porphyry copper deposits in southern Tibet triggered by subduction of the Indian continental plate. *SEG Spec. Publ.* **19**, 279–300 (2016).
6. Turner, S. et al. Post-collision, shoshonitic volcanism on the Tibetan Plateau: implications for convective thinning of the lithosphere and the source of ocean island basalts. *J. Petrol.* **37**, 45–71 (1996).
7. Zhao, Z. et al. Geochemical and Sr-Nd-Pb-O isotopic compositions of the post-collisional ultrapotassic magmatism in SW Tibet: petrogenesis and implications for India intra-continental subduction beneath southern Tibet. *Lithos* **113**, 190–212 (2009).
8. Guo, Z. & Wilson, M. Late Oligocene–early Miocene transformation of postcollisional magmatism in Tibet. *Geology* **47**, 776–780 (2019).
9. Foley, S. & Peccerillo, A. Potassic and ultrapotassic magmas and their origin. *Lithos* **28**, 181–185 (1992).
10. Liu, C. Z., Wu, F. Y., Chung, S. L. & Zhao, Z. D. Fragments of hot and metasomatized mantle lithosphere in Middle Miocene ultrapotassic lavas, southern Tibet. *Geology* **39**, 923–926 (2011).
11. Prelević, D., Jacob, D. E. & Foley, S. F. Recycling plus: a new recipe for the formation of Alpine–Himalayan orogenic mantle lithosphere. *Earth Planet. Sci. Lett.* **362**, 187–197 (2013).
12. Miller, C., Schuster, R., Klötzli, U., Frank, W. & Purtscheller, F. Post-collisional potassic and ultrapotassic magmatism in SW Tibet: geochemical and Sr–Nd–Pb–O isotopic constraints for mantle source characteristics and petrogenesis. *J. Petrol.* **40**, 1399–1424 (1999).
13. Peccerillo, A., Federico, M., Barbieri, M., Brilli, M. & Wu, T. W. Interaction between ultrapotassic magmas and car-bonate rocks:

evidence from geochemical and isotopic (Sr, Nd, O) compositions of granular lithic clasts from the Alban Hills Volcano, Central Italy. *Geochim. Cosmochim. Acta* **74**, 2999–3022 (2010).
14. Liu, D., Zhao, Z., Zhu, D. C., Niu, Y. & Harrison, T. M. Zircon xenocrysts in Tibetan ultrapotassic magmas: imaging the deep crust through time. *Geology* **42**, 43–46 (2013).
15. Li, W., Yang, Z., Chiaradia, M., Zhou, L. & Hou, Z. Enrichment nature of ultrapotassic rocks in southern Tibet inherited from their mantle source. *J. Petrol.* **62**, egab060 (2021).
16. Pilet, S., Baker, M. B. & Stolper, E. M. Metasomatized lithosphere and the origin of alkaline lavas. *Science* **320**, 916–919 (2008).
17. Foley, S. F., Ezad, I. S., van der Laan, S. R. & Pertermann, M. Melting of hydrous pyroxenites with alkali amphiboles in the continental mantle: 1. Melting relations and major element compositions of melts. *Geosci. Front.* **13**, 101380 (2022).
18. Förster, M. W. et al. Sediment-peridotite reaction controls fore-arc metasomatism and arc magma geochemical signatures. *Geosciences* **11**, 372 (2021).
19. Wang, Y., Foley, S. F., Buhre, S., Soldner, J. & Xu, Y. Origin of potassic postcollisional volcanic rocks in young, shallow, blueschist-rich lithosphere. *Sci. Adv.* **7**, eabc0291 (2021).
20. Wang, R. et al. Xenoliths in ultrapotassic volcanic rocks in the Lhasa block: direct evidence for crust–mantle mixing and metamorphism in the deep crust. *Contrib. Mineral. Petrol.* **171**, 1–19 (2016).
21. Tollan, P. M. E., O'Neill, H. S. C., Hermann, J., Benedictus, A. & Arculus, R. J. Frozen melt–rock reaction in a peridotite xenolith from sub-arc mantle recorded by diffusion of trace elements and water in olivine. *Earth Planet. Sci. Lett.* **422**, 169–181 (2015).
22. Li, W. et al. Redox state of southern Tibetan upper mantle and ultrapotassic magmas. *Geology* **48**, 733–736 (2020).
23. Yaxley, G. M. & Green, D. H. Reactions between eclogite and peridotite: mantle refertilisation by subduction of oceanic crust. *Schweiz. Mineral. Petrogr. Mitt.* **78**, 243–255 (1998).
24. Ionov, D. A., Doucet, L. S., Xu, Y., Golovin, A. V. & Oleinikov, O. B. Reworking of Archean mantle in the NE Siberian craton by carbonatite and silicate melt metasomatism: evidence from a carbonate-bearing, dunite-to-websterite xenolith suite from the Obnazhennaya kimberlite. *Geochim. Cosmochim. Acta* **224**, 132–153 (2018).
25. Kelemen, P. B., Dick, H. J. & Quick, J. E. Formation of harzburgite by pervasive melt/rock reaction in the upper mantle. *Nature* **358**, 635–641 (1992).
26. Rampone, E., Piccardo, G. B., Vannucci, R. & Bottazzi, P. Chemistry and origin of trapped melts in ophioiitic peridotites. *Geochim. Cosmochim. Acta* **61**, 4557–4569 (1997).
27. Bodinier, J. L., Garrido, C. J., Chanefo, I., Bruguier, O. & Gervilla, F. Origin of pyroxenite–peridotite veined mantle by refertilization reactions: evidence from the Ronda peridotite (Southern Spain). *J. Petrol.* **49**, 999–1025 (2008).
28. Sun, C. & Liang, Y. Distribution of REE between clinopyroxene and basaltic melt along a mantle adiabat: effects of major element composition, water, and temperature. *Contrib. Mineral. Petrol.* **163**, 807–823 (2012).
29. Moyen, J. F. The composite Archaean grey gneisses: petrological significance, and evidence for a non-unique tectonic setting for Archaean crustal growth. *Lithos* **123**, 21–36 (2011).
30. Palme, H. & O'Neill, H. S. C. Cosmochemical estimates of mantle composition. *Treat. Geochem.* **2**, 1–38 (2002).
31. Jeffcoate, A. B. et al. Li isotope fractionation in peridotites and mafic melts. *Geochim. Cosmochim. Acta* **71**, 202–218 (2007).
32. Rudnick, R. L., Gao, S., Holland, H. D. & Turekian, K. K. Composition of the continental crust. *Geochim. Cosmochim. Acta* **3**, 1–64 (2003).
33. Zhao, W. et al. Tibetan plate overriding the Asian plate in central and northern Tibet. *Nat. Geosci.* **4**, 870 (2011).
34. Longerich, H. P., Jackson, S. E. & Gunther, D. Laser ablation inductively coupled plasma mass spectrometric transient signal data acquisition and analyte concentration calculation. *J. Anal. At. Spectrom.* **11**, 899–904 (1996).
35. Jochum, K. P. et al. MPIDING reference glasses for in situ microanalysis: new reference values for element concentrations and isotope ratios. *Geochem. Geophys. Geosyst.* **7**, 217–222 (2006).
36. Paton, C., Woodhead, J. D., Hergt, J. M., Phillips, D. & Shee, S. Strontium isotope analysis of kimberlitic groundmass perovskite via LA-MC-ICP-MS. *Geostand. Geoanal. Res.* **31**, 321–330 (2007).
37. Yang, Y. H., Wu, F. Y., Xie, L. W., Chu, Z. Y. & Yang, J. H. Re-evaluation of interferences of doubly charged ions of heavy rare earth elements on Sr isotopic analysis using multi-collector inductively coupled plasma mass spectrometry. *Spectrochim. Acta Part B Atomic Spectroscopy* **97**, 118–123 (2014).
38. Tong, X. et al. Accurate determination of Sr isotopic compositions in clinopyroxene and silicate glasses by LA-MC-ICP-MS. *Geostand. Geoanal. Res.* **40**, 85–99 (2016).
39. Prelević, D., Akal, C., Romer, R. L., Mertz-Kraus, R. & Helvacı, C. Magmatic response to slab tearing: constraints from the Afyon Alkaline Volcanic Complex, Western Turkey. *J. Petrol.* **56**, 527–562 (2015).
40. Raczek, I., Jochum, K. P. & Hofmann, A. W. Neodymium and strontium isotope data for USGS reference materials BCR-1, BCR-2, BHVO-1, BHVO-2, AGV-1, AGV-2, GSP-1, GSP-2 and eight MPI-DING reference glasses. *Geostand. News.* **27**, 173–179 (2003).
41. Pin, C. & Bassin, C. Evaluation of a strontium-specific extraction chromatographic method for isotopic analysis in geological materials. *Anal. Chim. Acta* **269**, 249–255 (1992).
42. Sun, S. S. & McDonough, W. F. Chemical and isotopic systematics of oceanic basalts: implications for mantle composition and processes. *Geol. Soc. Lond. Spec. Publ.* **42**, 313–345 (1989).
43. Coltorti, M., Bonadiman, C., Hinton, R. W., Siena, F. & Upton, B. G. J. Carbonatite metasomatism of the oceanic upper mantle: evidence from clinopyroxenes and glasses in ultramafic xenoliths of Grande Comore, Indian Ocean. *J. Petrol.* **40**, 133–165 (1999).
44. Yang, Z. M. et al. Oxidized sediment recycling as a driver for postsubduction porphyry copper formation. *Sci. Adv.* **11**, eadx4474 (2025).

Acknowledgements

This work was funded by the National Key Research and Development Program of China (2022YFC2903304), European Research Council Consolidator Grants 2019 (864792), Scientific Research Fund Project of BGRIMM Technology Group (No. JTKY202427822), and National Natural Science Foundation of China (42502042). No permissions were required for sampling. We thank Martignier Agathe, Bin Chen, Huawei Li, Yiwei Zhou and Letian Xie for their assistance on the experimental measurement. The manuscript greatly benefits from constructive feedback provided by Joseph Aslin, Feifei Zhang, Alireza Bahadori, and three anonymous reviewers.

Author contributions

Weikai Li and Zhiming Yang contributed to project conceptualisation, fieldwork, sample, data analysis, data interpretation, manuscript writing and editing. Zoltán Zajacz contributed to data analysis, data interpretation, and manuscript editing. Limin Zhou contributed to data analysis and manuscript editing. Zengqian Hou contributed to data interpretation and manuscript editing.

Competing interests

The authors declare no competing interests.

Additional information

Supplementary information The online version contains supplementary material available at https://doi.org/10.1038/s43247-025-02778-0.

Correspondence and requests for materials should be addressed to Zhiming Yang.

Peer review information *Communications Earth and Environment* thanks the anonymous reviewers for their contribution to the peer review of this work. Primary Handling Editors: Feifei Zhang and Alireza Bahadori. A peer review file is available.

Reprints and permissions information is available at http://www.nature.com/reprints

Publisher's note Springer Nature remains neutral with regard to jurisdictional claims in published maps and institutional affiliations.

Open Access This article is licensed under a Creative Commons Attribution-NonCommercial-NoDerivatives 4.0 International License, which permits any non-commercial use, sharing, distribution and reproduction in any medium or format, as long as you give appropriate credit to the original author(s) and the source, provide a link to the Creative Commons licence, and indicate if you modified the licensed material. You do not have permission under this licence to share adapted material derived from this article or parts of it. The images or other third party material in this article are included in the article's Creative Commons licence, unless indicated otherwise in a credit line to the material. If material is not included in the article's Creative Commons licence and your intended use is not permitted by statutory regulation or exceeds the permitted use, you will need to obtain permission directly from the copyright holder. To view a copy of this licence, visit http://creativecommons.org/licenses/by-nc-nd/4.0/.

© The Author(s) 2025